Inorganic Chemistry

Open Access
This article is licensed under CC-BY-NC-ND 4.0

pubs.acs.org/IC
Article

Interplay between Cation "Coloring" and Stereochemically Active Lone Pairs in $AgBiS_2$ Thin Films

Kristopher M. Koskela,[#] Anindya Pakhira,[#] Marissa J. Strumolo, Sarbajit Banerjee,[*] and Richard L. Brutchey[*]

Cite This: *Inorg. Chem.* 2025, 64, 10097−10105
Read Online
ACCESS | Metrics & More | Article Recommendations | Supporting Information

ABSTRACT: Solution-processed $AgBiS_2$ thin films were fabricated using novel thiol−amine precursor inks to investigate the stereochemical activity of Bi^{3+} $6s^2$ lone pairs and their impact on the structure. A dual-space analysis combining Bragg diffraction and hard X-ray photoelectron spectroscopy (HAXPES) revealed a rock salt-like average structure with local distortions linked to cation coloring. Density functional theory (DFT) and crystal orbital Hamilton population (COHP) analyses confirmed that local Bi-rich and Ag-rich nanodomains amplify stereochemical activity, whereas more mixed and cation-order nanodomains are less stereochemically active. This local, nanoscopic mixing of segregated and ordered domains would indeed explain an average $Fm\bar{3}m$ structure that is rock salt-like and that does not manifest the full anharmonicity and noncentrosymmetry evidenced in canonical structures with stereochemical expression. These findings provide insights into the local structural and electronic complexities governing the optoelectronic properties of $AgBiS_2$ thin films.

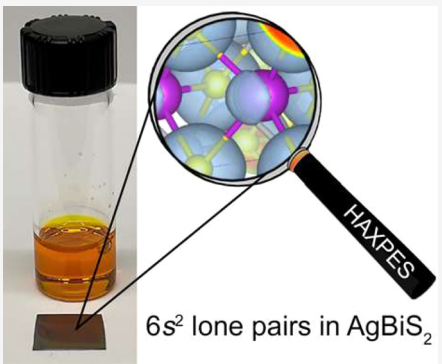

INTRODUCTION

Semiconductors containing post-transition metal, high-Z cations with ns^2 lone pairs are of significant interest because they can exhibit improved defect tolerance and/or self-healing,[1−4] soft polarizability,[5] higher carrier mobility from wider band dispersion,[6,7] enhanced dielectric constants for improved carrier transport,[8,9] and longer carrier lifetimes due to strong spin−orbit coupling.[10,11] Ionic lead halide perovskites belong to this broad class of semiconductors containing high-Z cations with ns^2 lone pairs; however, these materials are challenged by the presence of lead as a toxic heavy metal in addition to their environmental instability to ambient moisture and air. Beyond lead halide perovskites, a promising class of more covalent semiconductors is the ns^2-containing sulfosalts,[12] including such compositions as SnS,[13,14] Sb_2S_3,[15] Cu_3BiS_3,[16,17] and $CuPbSbS_3$.[18,19] It is proposed that such materials based on naturally occurring minerals will possess greater environmental stability than the lead halide perovskites. This ns^2-containing sulfosalt family of materials also includes the ternary I−V−VI_2 semiconductors that possess a rock salt-like structure.[20] A primary example of these rock salt-like I−V−VI_2 semiconductors is $AgBiS_2$, which is a known naturally occurring sulfosalt mineral named Schapbachite (Strunz 2.JA.15) that crystallizes in a cation-disordered average structure (space group $Fm\bar{3}m$).[21]

Solution-processed $AgBiS_2$ thin films have been utilized for photodetectors and ultrathin solar cells, which have been deposited using both precursor- and nanocrystal-based liquid inks.[22−28] While these solution-processed $AgBiS_2$ thin films have demonstrated promising performance metrics for optoelectronic devices, no work has been done to date to probe the nature and stereochemical expression of the Bi^{3+} $6s^2$ lone pair in thin films and whether this results in local, incoherent structural distortions about the Bi position. Herein, we report the solution deposition of $AgBiS_2$ thin films using novel thiol−amine-based precursor inks and present a dual-space analysis of the material to holistically describe the structure on both the average (with Bragg diffraction) and local (with hard X-ray photoelectron spectroscopy, or HAXPES) length scales. To examine the influence of the stereochemically active Bi^{3+} $6s^2$ lone pairs on cation configurations, we have probed the orbital character of states near the Fermi level using first-principles density functional theory (DFT) calculations. Furthermore, crystal orbital Hamilton population (COHP) analyses of pairwise bonding interactions and electron localization function (ELF) simulations have been performed to assign spectral features in the HAXPES and to examine the role of lone-pair-induced lattice anharmonicity in governing Ag- and Bi-ordering on the cation sublattice.

Received: February 14, 2025
Revised: April 17, 2025
Accepted: May 7, 2025
Published: May 13, 2025

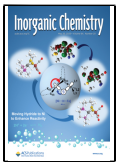

ACS Publications
© 2025 The Authors. Published by American Chemical Society

https://doi.org/10.1021/acs.inorgchem.5c00710
Inorg. Chem. 2025, 64, 10097−10105

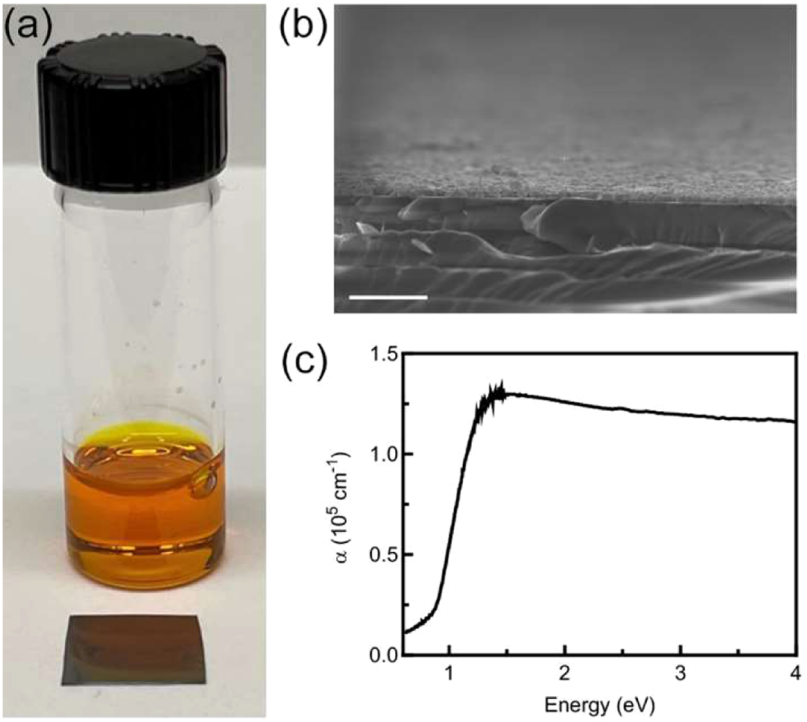

Figure 1. (a) Photograph of the orange precursor ink along with a representative example of a specularly reflective $AgBiS_2$ thin film. (b) Side-on SEM image of a 175 nm $AgBiS_2$ thin film deposited on Si at 35,000× (scale bar 2 μm). (c) Absorption coefficient of 175 nm $AgBiS_2$ thin film deposited on borosilicate glass.

EXPERIMENTAL METHODS

Thin Film Deposition. To formulate the precursor ink, 14.5 mg of Ag_2O (0.063 mmol; Alfa Aesar, 99%) and 32.2 mg of Bi_2S_3 (0.063 mmol; Sigma-Aldrich, 99.995%) were codissolved in 0.05 mL ethanedithiol (EDT; Alfa Aesar, 98+%) and 0.50 mL ethylenediamine (en; Sigma-Aldrich, 99.5%) under air with stirring at 30 °C overnight. Thin films were solution-processed by spin coating the resulting precursor ink onto *ca.* 1 cm^2 borosilicate glass substrates that were precleaned by consecutive bath sonication in methanol, acetone, and then isopropanol for 10 min each, followed by UV-ozone treatment for an additional 10 min. The ink was spin coated onto the substrate at 2500 rpm for 1 min under flowing nitrogen. The films were subsequently heated at *ca.* 15−20 °C/min to a set temperature of 400 °C, were annealed for 10 min under flowing nitrogen, and then allowed to cool naturally to 40 °C or lower. This was repeated three times for a total of three coats, which produced the 175 nm thin film.

Laboratory X-ray Diffraction. Powder X-ray diffraction patterns were collected using a Rigaku Ultima IV diffractometer operated at 44 mA and 40 kV, in the 2θ range of 10−70° using Cu $K\alpha$ radiation (λ = 1.5406 Å) with a step size and collection time of 0.01° and 3 s/step, respectively. All patterns were recorded under ambient conditions from powders that were produced by mechanically scraping the thin film from the substrate followed by grinding in an agate mortar and pestle. Rietveld refinements were carried out using the General Structure Analysis System II (GSAS-II) software package. The following parameters were refined: (1) scale factor, (2) background (modeled using a shifted Chebyshev polynomial function), (3) peak shape, (4) lattice constant (a), (5) fractional atomic coordinates constrained by the site symmetry, (6) preferred orientation using a spherical harmonic model, and (7) isotropic thermal parameters for each chemical species.

Computational Details. Total energy electronic structure calculations were performed within the framework of density functional theory (DFT) as implemented in the Vienna Ab initio Simulation Package (VASP),[29] using periodic boundary conditions to represent a perfect solid. Initial model optimizations were performed using a projected augmented wave (PAW)[30] methodology along a generalized gradient approximation using the Perdew−Burke−Ernzerhof functional (GGA-PBE)[31,32] to account for the electronic exchange and correlation. Atom- and orbital-projected density of states were computed using the Heyd−Scuseria−Ernzerhof screen hybrid exchange and correlation functional, or HSE06.[33,34] This functional incorporates a 75%:25% combination of PBE:Hartree−Fock and a range separation of 0.2 Å, with the goal of addressing the considerable underestimation of the band gap when calculated using the PBE functional alone. The cation-segregated structure necessitated the creation of various supercells, which was accomplished by extending the unit cell along the z-direction, where one-half of the Bi/Ag sites were occupied by Ag atoms, whereas the other half were occupied by Bi atoms. Among these, a 1 × 4 × 8 supercell with 4 layers of Bi atoms followed by 4 layers of Ag atoms emerged as the optimal configuration successfully balancing computational efficiency while capturing the stereochemical activity of the lone pairs of electrons. A Γ-point centered reciprocal grid of 8 × 2 × 1 points was employed for structure relaxation of the segregated supercell structure. The relaxation criteria for the structures were fixed to when each Cartesian force component was less than 0.01 eV/Å, unless otherwise noted. A kinetic energy cutoff of 520 eV was used for the plane wave basis restriction. The projected density of states (pDOS) along with the COHP[35] was calculated using the software package Local Orbital Suite Toward Electronic-Structure Reconstruction (LOBSTER). The absolute charge spilling is lower than 1.46% for all the structures.

Hard X-ray Photoelectron Spectroscopy (HAXPES). Bi core-level and valence band spectra of the $AgBiS_2$ thin films were obtained using energy-variant HAXPES at 2 and 5 keV excitation energies. The HAXPES investigations were performed at the National Synchrotron Light Source II (NSLS-II) facility, Brookhaven National Laboratory, utilizing the SST-2 beamline. Measurements were conducted at incident photon energies of 2 and 5 keV, employing a double crystal monochromator allowing for photon energy selection; Si (111) crystals were used for 2 keV photon energy and Si (220) crystals were used for 5 keV. The spectrometer was operated with a pass energy of 500 eV and energy step size of 0.050 eV, with the analyzer positioned

https://doi.org/10.1021/acs.inorgchem.5c00710
Inorg. Chem. 2025, 64, 10097−10105

to align its axis with the polarization vector of the incident radiation. Energy calibration was established using the Fermi edge of a gold reference sample prior to experimental measurements. The measurements were performed across the thin film sample on a spot size of about 500 μm × 500 μm where the signal/noise ratio was highest. The HAXPES measurements are averaged over the cm^2 areas of the surface of the thin film; focusing to smaller spot sizes significantly reduces signal-to-noise at high incident energies and gives rise to considerable beam damage.

RESULTS AND DISCUSSION

We have previously reported on the remarkable ability of a binary thiol−amine (or "alkahest") solvent mixture to dissolve more than 100 different bulk metals, metal oxides, and metal chalcogenides that span the periodic table.[36,37] By drawing from this palette of materials, a wide range of solution-processable, multinary precursor inks can be formulated. Using a conceptually simple dissolve and recover approach, thin films can be solution-deposited from these precursor inks with curing and mild annealing. In the absence of other external chalcogen sources, the thiol component of the precursor ink acts as the sulfur source to produce metal sulfide thin films upon thermal decomposition at temperatures ≤ 400 °C.[38,39]

To formulate a precursor ink for $AgBiS_2$, bulk powders of Ag_2O and Bi_2S_3 were stoichiometrically mixed and codissolved in a 1:10 (v/v) solvent mixture of ethanedithiol (EDT) and ethylenediamine (en) at 30 °C, giving an overall concentration of ∼90 mg of total dissolved solids per mL of solvent. The resulting precursor ink can be described as an optically clear, bright orange, and free-flowing solution that does not scatter light (Figure 1a). The ink remained stable and precipitate-free when kept under ambient conditions for several days. Negative ion mode electrospray ionization mass spectrometry (ESI-(−)MS) was used to elucidate the identity of the molecular solutes present in the composite precursor ink. The highest intensity peaks at m/z = 332.92 and 392.93 can be assigned to $[Bi(EDT^*)S]^-$ and $[Bi(EDT^*)_2]^-$, respectively, where EDT* is the doubly deprotonated dithiolate (Figure S1). The presence of m/z peaks corresponding to analogous silver thiolate complexes are also present but have much lower intensities that may be a result of differences in ionization. Interestingly, the m/z peak at 892.76 can be assigned to a bimetallic species with the formula $[AgBi(EDT^*)_4]^-$. Different combinations of bulk oxide and sulfide powders (i.e., Ag_2O, Bi_2O_3, Ag_2S, and Bi_2S_3) can also be used to formulate the ink and return $AgBiS_2$; however, Ag_2O and Bi_2S_3 were chosen due to these solids producing a precursor ink that yielded qualitatively higher-quality thin films lacking pinholes, edge defects, and microcracks, as visually assessed by light microscopy.

Thermogravimetric analysis returned an onset of volatilization and decomposition of the cured ink at *ca.* 120 °C that terminates between 350 and 400 °C (Figure S2). The end point of volatilization and decomposition of the cured ink was corroborated by the annealed thin film being completely devoid of IR bands that would correspond to organic species from the thiol−amine solvent system and the molecular solutes (Figure S3). Using this as a guide, the as-prepared precursor ink was spin coated onto substrates, cured, and annealed to 400 °C under flowing nitrogen to yield $AgBiS_2$ thin films. The resulting dark gray thin films were smooth, as evidenced by their specular reflectance, and were free of microcracks and pinholes (Figure 1a). Scanning electron microscopy was used to determine an average film thickness of 175 nm for the films studied herein (Figure 1b). Based on SEM images of the thin films, the films are comprised of irregularly shaped grains with an average height of 175 nm and an average width of 245 nm. Grain size calculated from the Scherrer broadening of the X-ray diffraction (XRD) pattern of the thin film is in general agreement with these values. The diffuse reflectance UV−vis-NIR spectrum of the resulting thin films gave a clean absorption edge corresponding to a direct allowed optical band gap of *ca.* 1.0 eV with an absorption coefficient of $\alpha = 10^5$ cm^{-1} reached by 1.4 eV (Figure 1c).[40−42] The absorption coefficient is consistent with the high optical absorption behavior of other bismuth-based chalcogenide semiconductors.[43] Energy dispersive X-ray spectroscopy revealed that the composition of the thin films was 1.3:0.7:2.0 Ag/Bi/S resulting from the stoichiometric precursor ink (Ag_2O/Bi_2S_3 = 1.0); off-stoichiometry is thermodynamically allowed for the cubic $Fm\bar{3}m$ average structure of $AgBiS_2$.[44] Schapbachite has been reported to have Ag/Bi ratios both above and below 1.0 depending upon the mineral location;[45,46] however, this mineral naturally occurs as a solid solution with galena PbS. Phase-pure, solution-processed thin films of $AgBiS_2$ have previously been reported to have nonstoichiometric Ag/Bi ratios ranging from 1.2 to 0.25.[22] This material provides a canonical example of the "coloring problem" with Ag and Bi being disordered across the cation sublattice; we will consider different local scale cation configurations from low to high ordering in the subsequent sections.

The Raman spectrum of a thin film displayed a broad Raman band centered at 256 cm^{-1} with a lower-energy shoulder at *ca.* 230 cm^{-1} that correspond to the known Bi−S and Ag−S vibrational modes of $AgBiS_2$, respectively (Figure S4).[47,48] To probe the phase purity and average, long-range structure of the $AgBiS_2$ thin films, Rietveld refinements of the laboratory powder XRD data were performed. The Rietveld refinement of the diffraction pattern using the cubic structure with the $Fm\bar{3}m$ space group corresponding to disordered rock salt-like $AgBiS_2$ returned a lattice parameter of a = 5.6266(3) Å (Figure 2) that matches well to previous reports for bulk $AgBiS_2$ (a = 5.64 Å).[21] The refinement returned a G.O.F. of 2.14 and an wR of 8.96%. Refinements of the data using the low-temperature structure of $AgBiS_2$ with a trigonal $P\bar{3}m1$ space group would not converge. The lower-intensity reflections of the lower

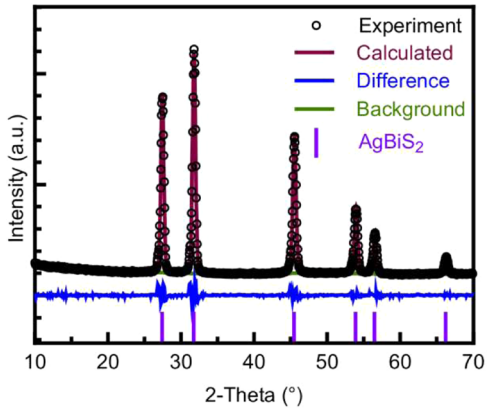

Figure 2. Rietveld refinement of laboratory powder X-ray diffraction data to the cubic $Fm\bar{3}m$ average structure of $AgBiS_2$. Open circles are experimental data, purple tick marks are individual reflections of the rock salt-like structure, and the difference pattern is given in blue (λ = 1.5406 Å, G.O.F. = 2.14, wR = 8.96%).

https://doi.org/10.1021/acs.inorgchem.5c00710
Inorg. Chem. 2025, 64, 10097−10105

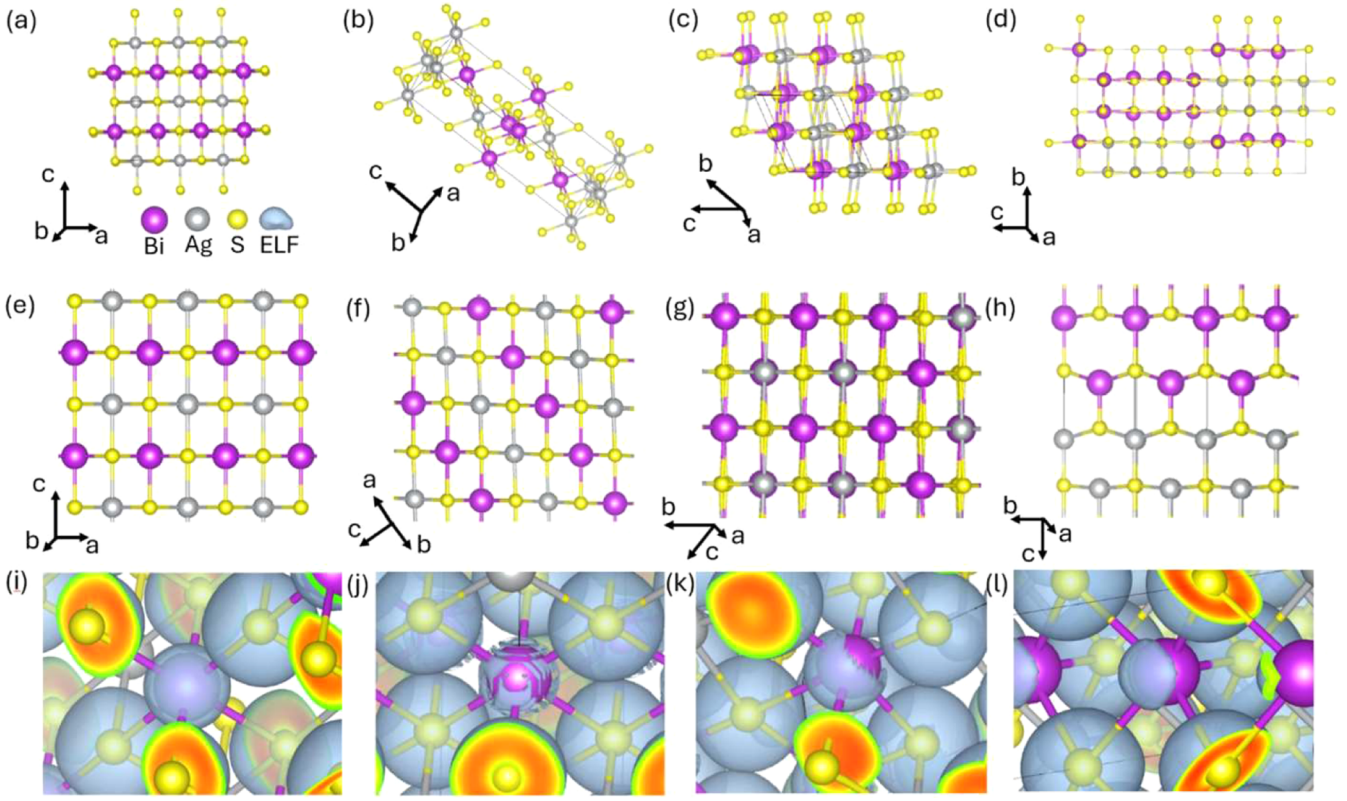

Figure 3. Unit cells for (a) *P*4/*mmm*, (b) *R*$\bar{3}$*m*, and (c) *Cc* space groups and (d) phase-segregated crystal structure renditions of $AgBiS_2$. Orientations showing cation ordering motifs of Ag and Bi atoms for (e) *P*4/*mmm*, (f) *R*$\bar{3}$*m*, and (g) *Cc* space groups and (h) phase-segregated crystal structures. ELF maps showing the change in electron localization as the structure changes from a disordered to a more segregated form, which illustrate the gradual and increasing expression of stereochemically active lone pairs on Bi^{3+} centers going from (i) *P*4/*mmm*, (j) *R*$\bar{3}$*m*, (k) *Cc*, to (l) phase-segregated structures.

symmetry trigonal structure are noticeably absent in our diffraction data (Figure S5). Furthermore, the refinement was not improved by the addition of the other thermodynamically stable ternary composition (i.e., $AgBi_3S_5$) or binary phases of Ag_2S or Bi_2S_3 that have plagued other solution-processed $AgBiS_2$ thin films,[49,50] confirming the phase purity of these thin films.

$AgBiS_2$ presents a complex structural challenge owing to the partial occupancies of Ag and Bi atoms on shared crystallographic sites. This "coloring problem" gives rise to local variations in cation positioning and can manifest segregated domains,[27] which significantly influence chemical bonding, local electronic structure, and are anticipated in this case to be strongly modified by and influence the stereochemical expression of Bi^{3+} $6s^2$ lone pairs.[51] Understanding how these structural variations affect material properties necessitates a systematic exploration of plausible atomic arrangements, capturing both ordered and disordered configurations. The coloring problem framework provides a crystallographic basis for addressing this challenge.[52] This approach treats the lattice as a network of sites, where each site can be occupied by specific atoms—in this case, Ag or Bi—while satisfying certain constraints, such as stoichiometry and local coordination environments. By systematically varying site occupancies under these rules, the framework generates a broad set of structural configurations, ranging from fully ordered alternating cation arrangements to locally segregated patterns. Sampling from the various structures that can be generated using this framework, we examine how the general configuration type modifies the degree of stereochemical activity of the Bi^{3+} $6s^2$ lone pairs;[6,53] the viability of different cation configurations is evaluated by comparison to HAXPES data based on the expression of stereochemically active lone pairs in $AgBiS_2$.

The four structural configurations examined here are chosen to capture a range of cation configurations in $AgBiS_2$. The first structure, corresponding formally to *P*4/*mmm*,[54] has alternating Bi and Ag atoms arranged along the *a*- and *b*-axes, which leads to distinct layers of Ag and Bi along the *c*-direction (Figure 3a,e). Such a configuration creates a regular alternate layered ordering of the two cations. In the second structure under consideration, which corresponds to a *R*$\bar{3}$*m* space group,[54] the Bi and Ag atoms are stacked in alternating layers, with each layer shifted by one unit cell along the *a*- or *b*-axes (Figure 3b,f). This arrangement also yields alternating layers of Ag and Bi atoms, but with a different stacking direction, which represents another variation of local symmetry and cation configurations. The third structure, representing a *Cc* space group,[54] features a more complex pattern where two rows of Bi atoms are followed by two rows of Ag atoms (Figure 3c,g), which thereby marks a deviation from simple single-layer stacking. This configuration yields a mixed arrangement of Bi and Ag atoms rather than distinct layers, which thus represents a variation with nonlayered alternating configurations. The fourth structure, denoted here as phase-segregated,[27] represents the bookend corresponding to complete segregation, with one-half of the Ag/Bi lattice sites in the unit cell occupied entirely by Ag atoms and the other half occupied by Bi atoms (Figure 3d,h). This model allows for the examination of the

https://doi.org/10.1021/acs.inorgchem.5c00710
Inorg. Chem. 2025, 64, 10097−10105

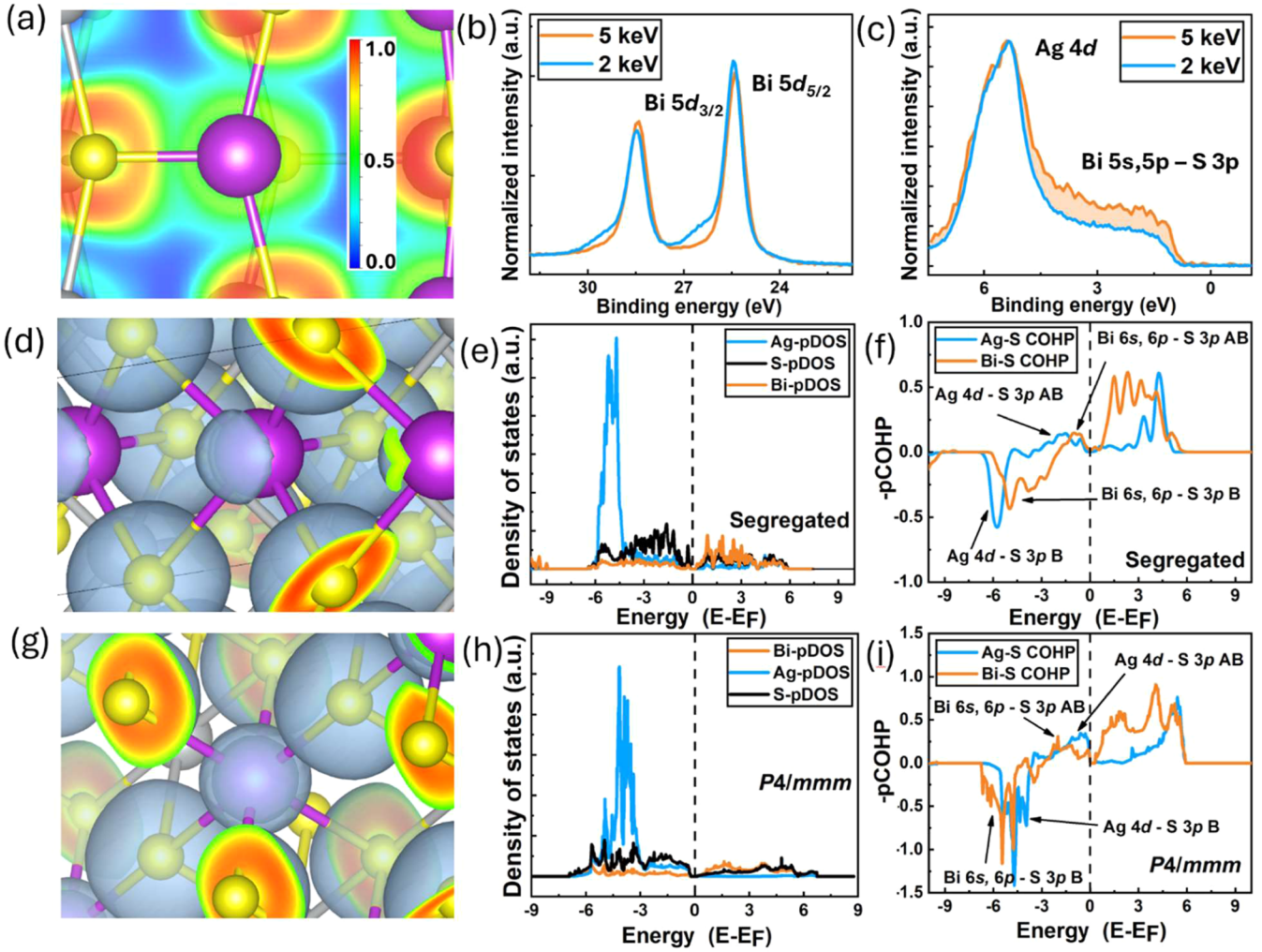

Figure 4. (a) ELF map along the (010) plane for the phase-segregated structure with 1.0 representing full localization, 0.5 representing uniform electron density, and 0 representing complete delocalization. (b) Energy-variant HAXPES acquired at 2 keV (blue) and 5 keV (orange) excitation for $AgBiS_2$. (c) Valence-band HAXPES showcasing the increase in intensity at valence-band maxima (VBM) with increasing excitation energy. (d) ELF map for the cation-segregated structure highlighting the stereochemically active lone pairs on Bi centers. (e) Atom-projected DOS for Ag, Bi, and S for the phase-segregated structure. (f) Ag−S pCOHP (blue) and Bi−S pCOHP (orange) plots for the cation-segregated structure. (g) ELF map for the ordered *P*4/*mmm* structure highlighting the symmetrical nature of electron localization. (h) Atom-projected DOS for the *P*4/*mmm* structure. (i) Ag−S pCOHP (blue) and Bi−S pCOHP (orange) for the *P*4/*mmm* structure.

effects of local segregation into nanoscopic domains, such as would be a result of a formal localized spinodal decomposition process.[55,56] Together, these configurations survey a spectrum of local cation arrangements, from highly ordered to fully segregated, enabling systematic examination of how varying degrees of cation ordering and segregation influence the electronic structure, bonding interactions, and stereochemical activity of the Bi^{3+} $6s^2$ lone pairs.

To probe the stereochemical expression and potential influence of the Bi^{3+} $6s^2$ lone pair on the local structure of the $AgBiS_2$ thin films, ELF maps have been computed using first-principles DFT, as shown in Figure 3i–l, and using energy-variant HAXPES, which has been interpreted with the aid of density of states (DOS) calculations and COHP analyses, as shown in Figure 4. The ELF maps indicate considerable distortion of electron density in the vicinity of Bi^{3+} centers in going from ordered, alternating Bi/Ag arrangements to cation-segregated Bi and Ag domains. The distortion reflects the increasing polarization of stereochemically expressed lone pairs.[53] The ELF maps illustrate that complete and ordered cation mixing suppresses stereochemical activity, whereas energetically proximate configurations with nanoscopic domains will enable manifestation of such stereochemical activity, and as a result, drive pronounced lattice anharmonicity.

We next use HAXPES to interrogate the formal valence and orbital contributions at the valence-band edge. The HAXPES core-level features observed at binding energies of 27 and 15 eV (Figure 4b) correspond to the Bi $5d_{3/2}$ and Bi $5d_{5/2}$ core levels, respectively, indicating a formal +3 oxidation state for Bi centers. Broad features, "fronting", above the baseline proximity of the Bi^{3+} $5d_{3/2}$ and Bi $5d_{5/2}$ core levels can be ascribed to either surface oxidation (since the films are processed in air) or the screening of core holes by conduction electrons. At 2 keV, the inelastic mean free path (IMFP) of the photoelectrons is *ca.* 3−8 nm, whereas at 5 keV, the IMFP is *ca.* 10−20 nm.[57] The close similarity in HAXPES core-level spectra at 2 and 5 keV excitations attest to the homogeneity of the solution-deposited thin films. Notably, the higher energy features are not observed at 5 keV. As photoelectrons travel

https://doi.org/10.1021/acs.inorgchem.5c00710
Inorg. Chem. 2025, 64, 10097−10105

through the material, they lose energy due to inelastic scattering, which results in the peaks appearing at a higher apparent binding energy. This effect is particularly amplified in materials with a high concentration of free charge carriers. Indeed, such "fronting" has also been observed for $CuBiS_2$. At 5 keV, however, the increased kinetic energy of the photoelectrons makes this effect somewhat less prominent. The higher energy of these features as compared to trivalent Bi^{3+} core-level features rules out contributions from zerovalent Bi^0.

Valence band HAXPES spectra provide information about the occupied density of states weighted by the photoionization cross sections (PICs) of the contributing orbitals.[58,59] While PICs decay rapidly with increasing incident photon energy, this effect is muted for ns^2-derived states because the PIC of the s orbital decreases more slowly as compared to orbitals with higher angular momentum quantum numbers. In this way, comparing the valence-band spectra excited by two different photon energies can identify the orbital contributions of ns^2 states at the Fermi level.

Valence-band HAXPES spectra collected at two distinct incident energies (2 and 5 keV) plotted in Figure 4c exhibit subtle differences at the valence-band maximum (VBM). An increase in relative intensity at the VBM upon 5 keV excitation reflects the predominant contributions of s- and p-states.[60,61] The contribution of these orbitals to HAXPES spectra at 2 keV is minimal, which is similarly observed as a marked loss in intensity at the top of the valence band. Based on atom-projected DOS and COHP analyses for the phase-segregated and cation-ordered configurations plotted in Figure 4 (see also Figure S6 in the Supporting Information), the valence band is derived primarily from Bi 6s, 6p and S 3p states hybridized with Ag 4d-states. DOS calculations shown in Figures 4 and S6 indicate that the extent to which Ag 4*d*-states are hybridized with S 3p and Bi 6s, p-states at the Fermi level is strongly dependent on the specifics of cation ordering in the structure.[27,54]

In the fully ordered, high-symmetry *P*4/*mmm* structure, COHP analyses reveal that Ag 4d−S 3p interactions dominate over Bi 6s, p−S 3*p* interactions at the VBM (Figure 4i).[35] In contrast, in the case of the phase-segregated structural model, the presence of Bi-rich and Ag-rich centers adjacent to each other gives rise to predominant Bi 6s, p−S 3p interactions as compared to Ag 4d-S 3p interactions at the VBM (Figure 4f). The intermediate structures display a continuum between these extremes (Figure S6), underscoring the sensitivity of the electronic structure to cation arrangement ("coloring"). The experimentally observed increase in intensity at the VBM at higher excitation energies is thus concordant with the greater stereochemical expression of Bi^{3+} $6s^2$ lone pairs as observed in the phase-segregated structural model. As per the revised lone pair model, hybridization with Bi 6p states facilitates a second-order Jahn−Teller distortion that stabilizes antibonding Bi 6s-S 3p derived orbitals at the VBM (which are selectively enhanced in intensity at 5 keV excitation in HAXPES).[62] ELF calculations presented in Figure 4a,d,g further support these findings, demonstrating a more pronounced localization of Bi 6s, p and S 3p states in the phase-segregated structure. This localization and asymmetry in the ELF map around a p-block cation is commonly observed in systems with strong stereochemical expression, which is manifested further as a pronounced local distortion of the crystal structure.[63,64] Notably, the magnitude of the intensity enhancement observed in Figure 4c is relatively modest, which suggests that the stereochemical activity of Bi $6s^2$-derived states is somewhat muted. This can be attributed to inhomogeneous cation ordering arrangements throughout the thin film such that Bi centers are stereochemically active in regions with cation segregation, whereas more mixed cation domains are stereochemically inactive, or "hidden". Valence band HAXPES provides an ensemble average across scores of nanoscopic domains. These nanoscale domains have very similar composition, varying only in their cation ordering or "coloring". Such nanoscopic domains do not show X-ray coherence (as evidenced by the narrow fwhm of reflections in Figure 2) and cannot be spatially resolved in HAXPES measurements, which have a spot size of several hundred microns.

The different cation "coloring" arrangements represent proximate local minima on the free energy landscape of Ag−Bi−S. In solution-phase processing, the limited energy available to the system constrains the extent to which it can explore the free energy landscape as it begins its descent toward (quasi)equilibrium states.[65,66] Such constrained processes effectively "trap" different cation configurations depending on spatiotemporal local thermal and strain gradients. Low-energy, semicoherent interfaces between domains with distinct "coloring" patterns can likely be stabilized; however, resolving distinct electronic structure features of individual domains will require higher spatial resolution measurements or stabilizing extended domains such as through epitaxial templating methods that enforce selective nucleation of a specific cation configuration.[65] It is indeed expected that extended domains with different cation configurations would manifest distinctive HAXPES valence-band spectra along the continuum from "inert" to fully expressed. Based on our observations, local, nanoscopic mixing of ordered and segregated domains would indeed explain an average $Fm\bar{3}m$ structure that is rock salt-like and that does not manifest the full anharmonicity and noncentrosymmetry evidenced in canonical *p*-block compounds with pronounced stereochemical expression, such as litharge or $FeSb_2O_4$.[7,62,64] Similarly, it has been shown that bulk ingots of $AgBiS_2$ appear to possess a $Fm\bar{3}m$ average structure by X-ray diffraction, while PDF analysis of synchrotron X-ray total scattering data of bulk $AgBiS_2$ is better fit to a *P*1 space group with a local structure comprised of cations offset from their octahedral centers. This local distortion was attributed to Bi $6s^2$ lone pairs.[67] More homogeneous cation ordering configurations in the thin films will require templated growth to reduce the nucleation barrier for a specific coloring motif or alleviation of thermal and strain gradients to access equilibrium configurations at a specific temperature.[65,68]

CONCLUSIONS

A combination of computational and experimental data suggest an intriguing local structural distortion at the boundary between Bi-rich and Ag-rich nanodomains in these $AgBiS_2$ thin films. As such, "hidden" in average $Fm\bar{3}m$ rock salt-like structure, local ordering of Ag and Bi atoms creates environments that modulate the expression of stereochemical activity. In particular, interfaces between Ag-rich and Bi-rich nanodomains amplify stereochemical activity, whereas other cation-ordered structural motifs suppress stereochemical expression to varying degrees. The observed electronic structure of $AgBiS_2$ thus reveals a delicate interplay between

https://doi.org/10.1021/acs.inorgchem.5c00710
Inorg. Chem. 2025, 64, 10097−10105

bonding interactions and structural ordering, particularly mediated by and affecting the stereochemical activity of Bi^{3+} $6s^2$ lone pairs. The solution-deposited $AgBiS_2$ thin films studied here comprise a mixture of structural configurations with varying degrees of cation segregation and resulting stereochemical expression. The study highlights how local inhomogeneities in "coloring" influence the electronic structure of $AgBiS_2$, offering valuable insights that may affect its functional behavior and potential applications in optoelectronics.

■ ASSOCIATED CONTENT

Supporting Information

The Supporting Information is available free of charge at https://pubs.acs.org/doi/10.1021/acs.inorgchem.5c00710.

Additional experimental details; mass spectrometry of precursor ink; TGA trace of ink decomposition; FT-IR spectra of cured precursor ink and annealed film; Raman spectrum of $AgBiS_2$ thin film; Rietveld refinement of diffraction data using the trigonal $P\bar{3}m1$ space group; atom-projected DOS and pCOHP for Cc and $R\bar{3}m$ structures (PDF)

■ AUTHOR INFORMATION

Corresponding Authors

Sarbajit Banerjee − *Department of Materials Science and Engineering, Texas A&M University, College Station, Texas 77845-3003, United States; Laboratory for Inorganic Chemistry, Department of Chemistry and Applied Biosciences, ETH Zurich, CH-8093 Zürich, Switzerland; Laboratory for Battery Science, PSI Center for Energy and Environmental Sciences, Paul Scherrer Institute, CH-5232 Villigen PSI, Switzerland;* orcid.org/0000-0002-2028-4675; Email: sbanerje@ethz.ch

Richard L. Brutchey − *Department of Chemistry, University of Southern California, Los Angeles, California 90089-3502, United States;* orcid.org/0000-0002-7781-5596; Email: brutchey@usc.edu

Authors

Kristopher M. Koskela − *Department of Chemistry, University of Southern California, Los Angeles, California 90089-3502, United States*

Anindya Pakhira − *Department of Chemistry, Texas A&M University, College Station, Texas 77845-3012, United States*

Marissa J. Strumolo − *Department of Chemistry, University of Southern California, Los Angeles, California 90089-3502, United States*

Complete contact information is available at: https://pubs.acs.org/10.1021/acs.inorgchem.5c00710

Author Contributions

#K.M.K. and A.P. contributed equally to this work.

Notes

The authors declare no competing financial interest.

■ ACKNOWLEDGMENTS

The thiol−amine precursor ink chemistry and laboratory characterization of the $AgBiS_2$ thin films was supported by the National Science Foundation under Award DMR-2418013 to R.L.B. A.P. and S.B. acknowledge support from the Welch Foundation under award A-1978-20190330. This research used resources of the National Synchrotron Light Source II, a U.S. Department of Energy (DOE) Office of Science User Facility operated for the DOE Office of Science by Brookhaven National Laboratory under contract DE-SC0012704. Portions of this research were conducted with the advanced computing resources provided by Texas A&M High Performance Research Computing.

■ REFERENCES

(1) Maughan, A. E.; Ganose, A. M.; Bordelon, M. M.; Miller, E. M.; Scanlon, D. O.; Neilson, J. R. Defect Tolerance to Intolerance in the Vacancy-Ordered Double Perovskite Semiconductors Cs_2SnI_6 and Cs_2TeI_6. *J. Am. Chem. Soc.* **2016**, *138*, 8453−8464.

(2) Caicedo-Dávila, S.; Cohen, A.; Motti, S. G.; Isobe, M.; McCall, K. M.; Grumet, M.; Kovalenko, M. V.; Yaffe, O.; Herz, L. M.; Fabini, D. H.; Egger, D. A. Disentangling the Effects of Structure and Lone-Pair Electrons in the Lattice Dynamics of Halide Perovskites. *Nat. Commun.* **2024**, *15*, No. 4184.

(3) Fabini, D. H.; Seshadri, R.; Kanatzidis, M. G. The Underappreciated Lone Pair in Halide Perovskites Underpins their Unusual Properties. *MRS Bull.* **2020**, *45*, 467−477.

(4) Balakrishnan, S. K.; Parambil, P. C.; Houben, L.; Asher, M.; Yaffe, O.; Edri, E. Revealing Hidden Phases and Self-Healing in Antimony Trichalcogenides and Chalcoiodides. *Cell Rep. Phys. Sci.* **2023**, *4*, No. 101298.

(5) Ogawa, K.; Abe, R.; Walsh, A. Band Gap Narrowing by Suppressed Lone-Pair Activity of Bi^{3+}. *J. Am. Chem. Soc.* **2024**, *146*, 5806−5810.

(6) Shi, J.; Rubinstein, E. A.; Li, W.; Zhang, J.; Yang, Y.; Lee, T.-L.; Qin, C.; Yan, P.; MacManus-Driscoll, J. L.; Scanlon, D. O.; Zhang, K. H. L. Modulation of the Bi^{3+} $6s^2$ Lone Pair State in Perovskites for High-Mobility p-Type Oxide Semiconductors. *Adv. Sci.* **2022**, *9*, No. 2104141.

(7) Handy, J. V.; Zaheer, W.; Rothfuss, A. R. M.; McGranahan, C. R.; Agbeworvi, G.; Andrews, J. L.; García-Pedraza, K. E.; Ponis, J. D.; Ayala, J. R.; Ding, Y.; Watson, D. F.; Banerjee, S. Lone but Not Alone: Precise Positioning of Lone Pairs for the Design of Photocatalytic Architectures. *Chem. Mater.* **2022**, *34*, 1439−1458.

(8) Sun, J.; Singh, D. J. Electronic Properties, Screening, and Efficient Carrier Transport in $NaSbS_2$. *Phys. Rev. Appl.* **2017**, *7*, No. 024015.

(9) Wang, X.; Li, Z.; Kavanagh, S. R.; Ganose, A. M.; Walsh, A. Lone Pair Driven Anisotropy in Antimony Chalcogenide Semiconductors. *Phys. Chem. Chem. Phys.* **2022**, *24*, 7195−7202.

(10) Tan, L. Z.; Rappe, A. M. Spin-Orbit Enhanced Carrier Lifetimes in Noncentrosymmetric Semiconductors. *J. Phys. Chem. Solids* **2019**, *128*, 225−230.

(11) Zheng, F.; Tan, L. Z.; Liu, S.; Rappe, A. M. Rashba Spin-Orbit Coupling Enhanced Carrier Lifetime in $CH_3NH_3PbI_3$. *Nano Lett.* **2015**, *15*, 7794−7800.

(12) Ganose, A. M.; Savory, C. N.; Scanlon, D. O. Beyond Methylammonium Lead Iodide: Prospects for the Emergent Field of ns^2 Containing Solar Absorbers. *Chem. Commun.* **2017**, *53*, 20−44.

(13) Sinsermsuksakul, P.; Sun, L.; Lee, S. W.; Park, H. H.; Kim, S. B.; Yang, C.; Gordon, R. G. Overcoming Efficiency Limitations of SnS-Based Solar Cells. *Adv. Energy Mater.* **2014**, *4*, No. 1400496.

(14) Antunez, P. D.; Buckley, J. J.; Brutchey, R. L. Tin and Germanium Monochalcogenide IV-VI Semiconductor Nanocrystals for Use in Solar Cells. *Nanoscale* **2011**, *3*, 2399−2411.

(15) Yang, W.; Zhang, X.; Tilley, S. D. Emerging Binary Chalcogenide Light Absorbers: Material Specific Promises and Challenges. *Chem. Mater.* **2021**, *33*, 3467−3489.

(16) Yakushev, M. V.; Maiello, P.; Raadik, T.; Shaw, M. J.; Edwards, P. R.; Krustok, J.; Mudryi, A. V.; Forbes, I.; Martin, R. W. Electronic and Structural Characterisation of Cu_3BiS_3 Thin Films for the Absorber Layer of Sustainable Photovoltaics. *Thin Solid Films* **2014**, *562*, 195−199.

(17) Koskela, K. M.; Tadle, A. C.; Chen, K.; Brutchey, R. L. Solution Processing Cu_3BiS_3 Absorber Layers with a Thiol-Amine Solvent Mixture. *ACS Appl. Energy Mater.* **2021**, *4*, 11026−11031.
(18) Koskela, K. M.; Melot, B. C.; Brutchey, R. L. Solution Deposition of a Bournonite $CuPbSbS_3$ Semiconductor Thin Film from the Dissolution of Bulk Materials with a Thiol-Amine Solvent Mixture. *J. Am. Chem. Soc.* **2020**, *142*, 6173−6179.
(19) Chang, E. T.; Koknat, G.; McKeown Wessler, G. C.; Yao, Y.; Blum, V.; Mitzi, D. B. Phase Stability, Band Gap Tuning, and Rashba Splitting in Selenium-Alloyed Bournonite: $CuPbSb(S_{1-x}Se_x)_3$. *Chem. Mater.* **2023**, *35*, 595−608.
(20) Medina-Gonzalez, A. M.; Yox, P.; Chen, Y.; Adamson, M. A. S.; Rosales, B. A.; Svay, M.; Smith, E. A.; Schaller, R. D.; Wu, K.; Rossini, A. J.; Kovnir, K.; Vela, J. Solution-Grown Ternary Semiconductors: Nanostructuring and Stereoelectronic Lone Pair Distortions in I-V-VI_2 Materials. *Chem. Mater.* **2022**, *34*, 7357−7368.
(21) Geller, S.; Wernick, J. H. Ternary Semiconducting Compounds with Sodium Chloride-Like Structure: $AgSbSe_2$, $AgSbTe_2$, $AgBiS_2$, $AgBiSe_2$. *Acta Crystallogr.* **1959**, *12*, 46−54.
(22) Ha, N.; Lee, G.; Park, J.; Lee, J.-H.; Jung, J.; Barma, S. V.; Kim, J.; Kim, J. H.; Kim, J. K.; Kwon, S. J.; Lee, S. U.; Jeong, S.; Lo, S. B.; Lee, J.-W.; Yang, W. Dithiocarbamate-Based Solution Processing for Cation Disorder Engineering in $AgBiS_2$ Solar Absorber Thin Films. *Adv. Energy Mater.* **2024**, *15*, No. 2402099.
(23) Gu, E.; Lin, X.; Tang, X.; Matt, G. J.; Osvet, A.; Hou, Y.; Jäger, S.; Xie, C.; Karl, A.; Hock, R.; Brabec, C. J. Single Molecular Precursor Ink for $AgBiS_2$ Thin Films: Synthesis and Characterization. *J. Mater. Chem. C* **2018**, *6*, 7642−7651.
(24) Burgués-Ceballos, I.; Wang, Y.; Konstantatos, G. Mixed $AgBiS_2$ Nanocrystals for Photovoltaics and Photodetectors. *Nanoscale* **2022**, *14*, 4987−4993.
(25) Li, Z.; Zhang, G.; Li, Z.; Xie, Y.; Xia, Y.; Hu, Z.; Chao, L.; Wang, F.; Chen, Y. Precisely Tailoring the Precursor Solution for Efficient $AgBiS_2$ Solar Cells. *CrystEngComm* **2024**, *26*, 3026−3032.
(26) Kelley, M. L.; Ahmed, F.; Abiodun, S. L.; Usman, M.; Jewel, M. U.; Hussain, K.; zur Loye, H.-C.; Chandrashekhar, M. V. S.; Greytak, A. B. Photoconductive Thin Films Composed of Environmentally Benign $AgBiS_2$ Nanocrystal Inks Obtained through a Rapid Phase Transfer Process. *ACS Appl. Electron. Mater.* **2021**, *3*, 1550−1555.
(27) Wang, Y.; Kavanagh, S. R.; Burgués-Ceballos, I.; Walsh, A.; Scanlon, D. O.; Konstantatos, G. Cation Disorder Engineering Yields $AgBiS_2$ Nanocrystals with Enhanced Optical Absorption for Efficient Ultrathin Solar Cells. *Nat. Photonics* **2022**, *16*, 235−241.
(28) van Embden, J.; Della Gaspera, E. Ultrathin Solar Absorber Layers of Silver Bismuth Sulfide from Molecular Precursors. *ACS Appl. Mater. Interfaces* **2019**, *11*, 16674−16682.
(29) Hafner, J. Ab-initio Simulations of Materials using VASP: Density-Functional Theory and Beyond. *J. Comput. Chem.* **2008**, *29*, 2044−2078.
(30) Maintz, S.; Deringer, V. K.; Tchougréef, A. L.; Dronskowski, R. Analytical Projection from Plane-Wave and PAW Wavefunctions and Application to Chemical-Bonding Analysis in Solids. *J. Comput. Chem.* **2013**, *34*, 2557−2567.
(31) Ziesche, P.; Kurth, S.; Perdew, J. P. Density Functionals from LDA to GGA. *Comput. Mater. Sci.* **1998**, *11*, 122−127.
(32) Perdew, J. P.; Burke, K.; Wang, Y. Generalized Gradient Approximation for the Exchange-Correlation Hole of a Many-Electron System. *Phys. Rev. B* **1996**, *54*, No. 16533.
(33) Krukau, A. V.; Vydrov, O. A.; Izmaylov, A. F.; Scuseria, G. E. Influence of the Exchange Screening Parameter on the Performance of Screened Hybrid Functionals. *J. Chem. Phys.* **2006**, *125*, No. 224106.
(34) Saßnick, H.-D.; Cocchi, C. Electronic Structure of Cesium-Based Photocathode Materials from Density Functional Theory: Performance of PBE, SCAN, and HSE06 Functionals. *Electron. Struct.* **2021**, *3*, No. 027001.
(35) Deringer, V. L.; Tchougréeff, A. L.; Dronskowski, R. Crystal Orbital Hamilton Population (COHP) Analysis as Projected from Plane-Wave Basis Sets. *J. Phys. Chem. A* **2011**, *115*, 5461−5466.
(36) Koskela, K. M.; Strumolo, M. J.; Brutchey, R. L. Progress of Thiol-Amine "Alkahest" Solutions for Thin Film Deposition. *Trends Chem.* **2021**, *3*, 1061−1073.
(37) McCarthy, C. L.; Brutchey, R. L. Solution Processing of Chalcogenide Materials Using Thiol-Amine "Alkahest" Solvent Systems. *Chem. Commun.* **2017**, *53*, 4888−4902.
(38) McCarthy, C. L.; Webber, D. H.; Schueller, E. C.; Brutchey, R. L. Solution-Phase Conversion of Bulk Metal Oxides to Metal Chalcogenides Using a Simple Thiol-Amine Solvent Mixture. *Angew. Chem., Int. Ed.* **2015**, *54*, 8378−8381.
(39) Webber, D. H.; Brutchey, R. L. Alkahest for V_2VI_3 Chalcogenides: Dissolution of Nine Bulk Semiconductors in a Diamine-Dithiol Solvent Mixture. *J. Am. Chem. Soc.* **2013**, *135*, 15722−15725.
(40) Pejova, B.; Grozdanov, I.; Nesheva, D.; Petrova, A. Size-Dependent Properties of Sonochemically Synthesized Three-Dimensional Arrays of Close-Packed Semiconducting $AgBiS_2$ Quantum Dots. *Chem. Mater.* **2008**, *20*, 2551−2565.
(41) Pejova, B.; Nesheva, D.; Aneva, Z.; Petrova, A. Photoconductivity and Relaxation Dynamics in Sonochemically Synthesized Assemblies of $AgBiS_2$ Quantum Dots. *J. Phys. Chem. C* **2011**, *115*, 37−46.
(42) Chen, C.; Qiu, X.; Ji, S.; Jia, C.; Ye, C. The Synthesis of Monodispersed $AgBiS_2$ Quantum Dots with a Giant Dielectric Constant. *CrystEngComm* **2013**, *15*, 7644−7648.
(43) Santos, D. R.; Shukla, S.; Vermang, B. Prospects of Copper-Bismuth Chalcogenide Absorbers for Photovoltaics and Photoelectrocatalysis. *J. Mater. Chem. A* **2023**, *11*, 22087−22104.
(44) Tesfaye, F.; Linderberg, D. Thermochemical Properties of Selected Ternary Phases in the Ag-Bi-S System. *J. Mater. Sci.* **2016**, *51*, 5750−5759.
(45) Staude, S.; Dorn, A.; Pfaff, K.; Markl, G. Assemblages of Ag-Bi Sulfosalts and Conditions of their Formation: The Type Locality of Schapbachite ($Ag_{0.4}Pb_{0.2}Bi_{0.4}S$) and Neighboring Mines in the Schwarzwald Ore District, Southern Germany. *Can. Mineral.* **2010**, *48*, 441−446.
(46) Walenta, K.; Bernhardt, H.-J.; Theye, T. Cubic $AgBiS_2$ (Schapbachite) from the Silberbrünnle Mine near Gengenbach in the Central Black Forest, Germany. *Neues Jahrb. Mineral., Monatsh.* **2004**, *2004*, 425−432.
(47) Guin, S. N.; Banerjee, S.; Danyal, D.; Pati, S. K.; Biswas, K. Origin of the Order-Disorder Transition and the Associated Anomalous Change of Thermopower in $AgBiS_2$ Nanocrystals: A Combined Experimental and Theoretical Study. *Inorg. Chem.* **2016**, *55*, 6323−6331.
(48) Wu, Y.; Wan, L.; Zhang, W.; Li, X.; Fang, J. In Situ Grown Silver Bismuth Sulfide Nanorod Arrays and Their Application to Solar Cells. *CrystEngComm* **2019**, *21*, 3137−3141.
(49) Yao, F.; Jiang, L.; Qi, Y.; Li, R.; Li, Y.; Xu, Y.; Liu, H.; Lin, Q. Chemical Bath Deposition of $AgBiS_2$ Films for Visible and X-ray Detection. *Appl. Mater. Today* **2022**, *26*, No. 101262.
(50) Sugarthi, S.; Bakiyaraj, G.; Abinaya, R.; Navaneethan, M.; Arachana, J.; Shimomura, M. Effect of Different Growth Temperature on the Formation of Ternary Metal Chalcogenides $AgBiS_2$. *Mater. Sci. Semicond. Process.* **2020**, *107*, No. 104781.
(51) Miller, G. J. The "Coloring Problem" in Solids: How It Affects Structure, Composition and Properties. *Eur. J. Inorg. Chem.* **1998**, *5*, 523−536.
(52) Burdett, J. K.; Lee, S.; McLarnan, T. J. Coloring Problem. *J. Am. Chem. Soc.* **1985**, *107*, 3083−3089.
(53) Agbeworvi, G.; Zaheer, W.; Handy, J. V.; Andrews, J. L.; Perez-Beltran, S.; Jaye, C.; Weiland, C.; Fischer, D. A.; Balbuena, P. B.; Banerjee, S. Toggling Stereochemical Activity through Interstitial Positioning of Cations between 2D V_2O_5 Double Layers. *Chem. Mater.* **2023**, *35*, 7175−7188.
(54) Ju, M.-G.; Dai, J.; Ma, L.; Zhou, Y.; Zeng, X. C. $AgBiS_2$ as a Low-Cost and Eco-Friendly All-Inorganic Photovoltaic Material: Nanoscale Morphology-Property Relationship. *Nanoscale Adv.* **2020**, *2*, 770−776.

https://doi.org/10.1021/acs.inorgchem.5c00710
Inorg. Chem. 2025, 64, 10097−10105

(55) Orthacker, A.; Haberfehlner, G.; Taendl, J.; Poletti, M. C.; Sonderegger, B.; Kothleitner, G. Diffusion-Defining Atomic-Scale Spinodal Decomposition within Nanoprecipitates. *Nat. Mater.* **2018**, *17*, 1101−1107.
(56) Santos, D. A.; Rezaei, S.; Zhang, D.; Luo, Y.; Lin, B.; Balakrishna, A. R.; Xu, B.-X.; Banerjee, S. Chemistry-Mechanics-Geometry Coupling in Positive Electrode Materials: A Scale-Bridging Perspective for Mitigating Degradation in Lithium-Ion Batteries through Materials Design. *Chem. Sci.* **2023**, *14*, 458−484.
(57) Tanuma, S.; Powell, C. J.; Penn, D. R. Calculations of Electron Inelastic Mean Free Paths. IX. Data for 41 Elemental Solids over the 50 eV to 30 keV Range. *Surf. Interface Anal.* **2011**, *43*, 689−713.
(58) Kalha, C.; Fernando, N. K.; Bhatt, P.; Johansson, F. O. L.; Lindblad, A.; Rensmo, H.; Medina, L. Z.; Lindblad, R.; Siol, S.; Jeurgens, L. P. H.; Cancellieri, C.; Rossnagel, K.; Medjanik, K.; Schönhense, G.; Simon, M.; Gray, A. X.; Nemšák, S.; Lömer, P.; Schlueter, C.; Regoutz, A. Hard X-ray Photoelectron Spectroscopy: A Snapshot of the State-of-the-Art in 2020. *J. Phys.:Condens. Matter* **2021**, *33*, No. 233001.
(59) Artyushkova, K.; Leadley, S. R.; Shard, A. G. Introduction to Reproducible Laboratory Hard X-ray Photoelectron Spectroscopy. *J. Vac. Sci. Technol,. A* **2024**, *42*, No. 052801.
(60) Green, J. C.; Decleva, P. Photoionization Cross-Sections: A Guide to Electronic Structure. *Coord. Chem. Rev.* **2005**, *249*, 209−228.
(61) Weiland, C.; Rumaiz, A. K.; Lysaght, P.; Karlin, B.; Woicik, J. C.; Fischer, D. NIST High Throughput Variable Kinetic Energy Hard X-ray Photoelectron Spectroscopy Facility. *J. Electron Spectrosc. Relat. Phenom.* **2013**, *190*, 193−200.
(62) Walsh, A.; Payne, D. J.; Egdell, R. G.; Watson, G. W. Stereochemistry of Post-Transition Metal Oxides: Revision of the Classical Lone Pair Model. *Chem. Soc. Rev.* **2011**, *40*, 4455−4463.
(63) Walsh, A.; Watson, G. W. The Origin of the Stereochemically Active Pb(II) Lone Pair: DFT Calculations on PbO and PbS. *J. Solid State Chem.* **2005**, *178*, 1422−1428.
(64) Zaheer, W.; Andrews, J. L.; Parija, A.; Hyler, F. P.; Jaye, C.; Weiland, C.; Yu, Y.-S.; Shapiro, D. A.; Fischer, D. A.; Guo, J.; Velázquez, J. M.; Banerjee, S. Reversible Room-Temperature Fluoride-Ion Insertion in a Tunnel-Structured Transition Metal Oxide Host. *ACS Energy Lett.* **2020**, *5*, 2520−2526.
(65) Parija, A.; Waetzig, G. R.; Andrews, J. L.; Banerjee, S. Traversing Energy Landscapes Away from Equilibrium: Strategies for Accessing and Utilizing Metastable Phase Space. *J. Phys. Chem. C* **2018**, *122*, 25709−25728.
(66) Tappan, B. A.; Brutchey, R. L. Polymorphic Metastability in Colloidal Semiconductor Nanocrystals. *ChemNanoMat* **2020**, *6*, 1567−1588.
(67) Rathore, E.; Juneja, R.; Culver, S. P.; Minafra, N.; Singh, A. K.; Zeier, W. G.; Biswas, K. Origin of Ultralow Thermal Conductivity in n-Type Cubic Bulk $AgBiS_2$: Soft Ag Vibrations and Local Structural Distortion Induced by the Bi $6s^2$ Lone Pair. *Chem. Mater.* **2019**, *31*, 2106−2113.
(68) Sun, W.; Dacek, S. T.; Ong, S. P.; Hautier, G.; Jain, A.; Richards, W. D.; Gamst, A. C.; Persson, K. A.; Ceder, G. The Thermodynamic Scale of Inorganic Crystalline Metastability. *Sci. Adv.* **2016**, *2*, No. e1600225.

https://doi.org/10.1021/acs.inorgchem.5c00710
Inorg. Chem. 2025, 64, 10097−10105